1-29-2018

Exploiting Anisotropy of Plasmonic Nanostructures with Polarization-Modulation Infrared Linear Dichroism Microscopy (μPM-IRLD).

Gregory Q. Wallace
Western University

Stuart Read
Canadian Light Source

Danielle M. McRae
Western University

Scott Rosendhal
Canadian Light Source

Francois Lagugne-Labarthet
University of Western Ontario, flagugne@uwo.ca

DOI: 10.1002/ ((please add manuscript number))
Article type: Full Paper

Exploiting Anisotropy of Plasmonic Nanostructures with Polarization-Modulation Infrared Linear Dichroism Microscopy (μPM-IRLD).

*Gregory Q. Wallace, Stuart T. Read, Danielle M. McRae, Scott M. Rosendahl, and François Lagugné-Labarthet**

G. Q. Wallace, D. M. McRae, Prof. F. Lagugné-Labarthet
Department of Chemistry and the Centre for Advanced Materials and Biomaterials Research
University of Western Ontario
1151 Richmond Street, London, Ontario
N6A 5B7, Canada
E-mail: flagugne@uwo.ca

Dr. S. T. Read, Dr. S. M. Rosendahl
Canadian Light Source Inc.
44 Innovation Boulevard, Saskatoon, Saskatchewan
S7N 2V3, Canada

Keywords: plasmonics, polarization-modulation, linear dichroism, dendritic fractals, SEIRA

Metallic nanostructures that exhibit plasmon resonances in the mid-infrared range are of particular interest for a variety of optical processes where the infrared excitation and/or emission could be enhanced. This plasmon-mediated enhancement can potentially be used towards highly sensitive detection of an analyte(s) by techniques such as surface-enhanced infrared absorption (SEIRA). To maximize the SEIRA enhancement, it is necessary to prepare highly tuned plasmonic resonances over a defined spectral range that can span over several microns. Noteworthy, nanostructures with anisotropic shapes exhibit multiple resonances that can be exploited by controlling the polarization of the input light. This study demonstrates the role of polarization-modulation infrared linear dichroism coupled to microscopy measurements (μPM-IRLD) as a powerful means to explore the optical properties of anisotropic nanostructures. Quantitative μPM-IRLD measurements were conducted on a

series of dendritic fractals as model structures to explore the role of structural anisotropy on the resulting surface-enhanced infrared absorption and sensing application. Once functionalized with an analyte, the μPM-IRLD SEIRA results highlight that it is possible to selectively enhance further vibrational modes of analytes making use of the structural anisotropy of the metallic nanostructure.

1. Introduction

Polarized light can be readily used to probe the orientation, and anisotropy of molecular systems, including thin films,[1, 2] proteins,[3, 4] and self-assembled monolayers.[5-7] When combined with microscopy, polarized light measurements can yield critical information about the orientation of crystallographic axes in microstructures or enable the ability to map the distribution of anisotropic domains.[8, 9] Raman,[10-12] infrared,[13, 14] and sum-frequency generation are examples of vibrational spectroscopies that yield molecular anisotropy information using a set of polarized measurements.[15-17] Noteworthy, polarized spectroscopic measurements can be of interest to probe metamaterials, such as plasmonic nanostructures, that exhibit an anisotropic response under polarized light.[18-23]

This anisotropic response can manifest itself in different ways. First, the spectral position of localized surface plasmon resonances (LSPRs) can be tuned to different spectral domains. Metallic nanorod arrays are a classical example of this where an LSPR can exist in the mid-IR for a polarization parallel to the long axis of the nanorod, and for a polarization perpendicular to the long axis, the LSPR lies in the visible region.[24] Second, the spatial distribution of nanoscale electromagnetic enhancement, known as hot-spots, can be tailored by changing the polarization of the input light.[25] These two plasmonic properties can be simultaneously exploited by correctly tailoring the opto-geometric properties of the nanostructure.[26]

Of the spectral domains of interest for vibrational spectroscopy, the mid-IR remains a significant challenge as it spans a domain of 2.5 to 20 μm (500-4000 cm^{-1}). Achieving a

single broad resonance that covers that entire range is incredibly difficult, thus alternative approaches are required to perform plasmon-enhanced measurements. By exploiting the anisotropic response of nanostructures and metasurfaces, it is possible to overcome the need for a single broad resonance by instead generating a series of polarization dependent resonances.[27-31] An advantage of this approach is that a given resonance or set of resonances can be individually tuned to a specific frequency,[32, 33] or frequencies,[34] and therefore individually excited with a given polarization. Structures that support multiple polarization dependent resonances can be applied to a variety of applications. These include: polarized plasmon-mediated surface chemistry where a surface is functionalized with different analytes using different polarizations,[35] or polarized optical filters with distinct polarization responses.[36, 37] An interesting, yet under explored aspect of anisotropic nanostructures is the differential absorbance, ΔA, that is associated with the dichroic (linear or circular) properties of the structure. By exploiting the improved sensitivity offered by a plasmon-enhanced ΔA measurement, the local molecular anisotropy of an adsorbed analyte can be probed.[38-40] Furthermore, it may be possible to induce local anisotropy to the analyte through the interaction between the adsorbed analyte and a locally polarized plasmon. Such a sensitive interaction could be used to favor molecular adsorption of chiral molecules using plasmonic structures with differential responses to left and right circularly polarized light.

In this study, we first explore the linear dichroic properties of plasmonic nanostructures using polarization modulation (PM) spectroscopy in the mid-IR spectral range. These measurements were performed on fractal gold nanostructures fabricated using electron-beam lithography and probed under microscopy conditions using a synchrotron mid-IR beam line (Canadian Light Source). In PM infrared spectroscopy, a photoelastic modulator (PEM) modulates the light between two linear orthogonal polarizations at high frequency. The collected differential signal is proportional to the differential absorption, ΔA, that can also be exploited to enhance the sensitivity of the plasmon-mediated spectroscopic measurement due

to the spectral and spatial anisotropy of the plasmon resonances. Specifically, micro polarization-modulation infrared linear dichroism (μPM-IRLD) measurements were conducted to probe adsorbed analytes on a series of dendritic fractal structures. The dendritic fractals were chosen as our model structure because they support multiple LSPRs together with a large density of hot-spots that are anisotropically distributed. Finite difference time domain (FDTD) calculations were performed to relate the spatial anisotropy of the structure to the dichroic infrared spectra. Since the tuning of the spectral position of the resonances is critical to the development of new plasmonic structures in the infrared range, we explore how altering the dimensions of the structure (size), configuration (number of inner branches), and number of resonances (generation of the fractal), changes the resulting differential set of calibrated spectra. Last, the platforms were functionalized with an analyte, so that a self-assembled monolayer was formed on the surface, and μPM-IRLD surface-enhanced infrared absorption (SEIRA) measurements could be performed. This study demonstrates an important development towards the understanding of polarization dependence of molecular systems by working with structures that exhibit polarization dependence.

2. Results and Discussion

2.1. Polarization Dependence of Dendritic Fractals

Inspired by the Cayley Tree fractal,[41] we have previously explored a more general version of radial fractals, classified as dendritic fractals.[42] For such structures, with each additional generation, a new lower energy (lower wavenumber) resonance is introduced. The spectral position of the resonance can then be tuned by altering the size, shape, and configuration of the fractal.[42] Since studies involving SEIRA emphasize the detection of small molecules, polymers, proteins, and lipids, the spectral regions between 1000 – 2000, and 2800 – 3200 cm^{-1} are of the greatest interest. Therefore, the design of the dendritic fractals was chosen such that resonance(s) would be in, or near those regions.

For this study, the focus was placed on the second-order generation structure. To highlight the polarization dependence of the structure, a three-branched dendritic fractal was chosen (**Figure 1A**). The side length of the nanorods was written as 350 nm because based on our previous study, such dimensions would provide resonances near the relevant spectral regions. When probed, the structurally tailored fractal exhibited two resonances between 1200 and 3500 cm^{-1} (**Figure 1B**). Additionally, the spectral positions of the resonances measured with orthogonal polarizations exhibit a slight polarization dependence as shown by the spectral shifts observed between the spectra obtained at 0 and 90 degrees.

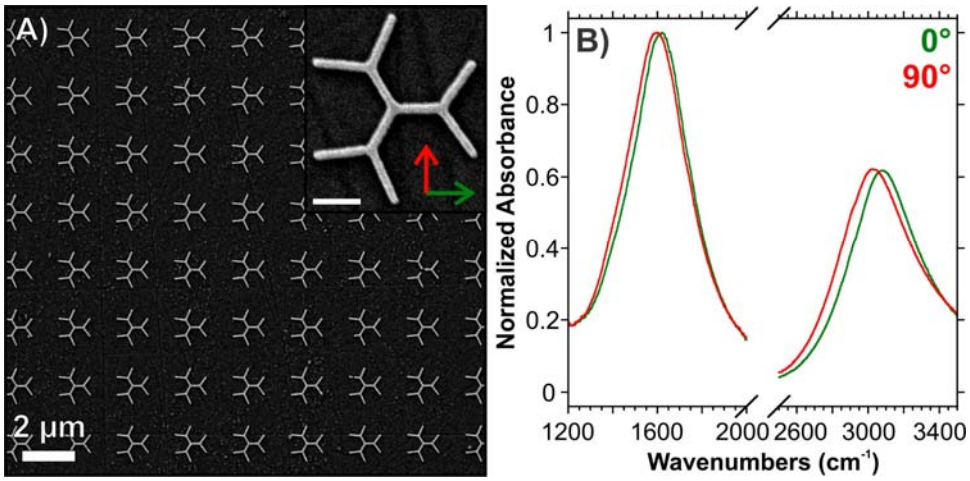

Figure 1. A) Scanning electron micrograph of three-branched second-order generation dendritic fractals prepared by electron-beam lithography. B) Experimental absorbance spectra obtained using orthogonal polarizations on the same sample as A). The scale bar on the inset SEM image is 350 nm. The arrows in the inset correspond to the polarization directions reported in A).

2.2. Polarization-Modulated Measurements of Dendritic Structures

Polarization modulation (PM) infrared spectroscopy is a technique of choice to probe a variety of surfaces and interfaces in reflection and transmission modes, revealing the molecular orientation at the monolayer level.[43-48] Linear dichroism can be measured with high accuracy over a large spectral range using polarization modulation spectroscopy that

yields the differential absorption measurement $\Delta A = A_{0°} - A_{90°}$, where $A_{0°}$ and $A_{90°}$ are the absorbances along the two orthogonal polarizations. The value of ΔA can then be exploited to determine the orientation of vibrational modes through the measurement of their anisotropy.

Most infrared PM measurements have been conducted macroscopically, where the infrared beam that emerges from the infrared interferometer is focused with a long focal lens onto the sample surface. By coupling the PM measurements with a microscope and a synchrotron source, it is possible to obtain spatially resolved measurements of the linear dichroism with a typical spatial resolution slightly better than 10 μm.[49] Such μPM-IRLD measurements have been applied to a very limited number of systems to determine hydrogen bonding and orientation in wood polymer fibres,[50] and the anisotropy of crystalline or semicrystalline domains.[51, 52] To the best of our knowledge, no previous studies have coupled this approach with plasmonic nanostructures.

For arrays of nanostructures prepared by electron-beam lithography, the dimensions of the individual arrays are typically limited to between 50 × 50 μm^2 and 100 × 100 μm^2 (50 × 50 μm^2 for this study) and are further arranged into grids. Thus, to probe the anisotropic response of an individual structure, a field of view of 50 × 50 μm^2 is necessary and must involve the coupling of PM-IRLD with an IR-compatible microscope. Performing classical absorbance measurements with the PEM provides the average absorbance, $A_{ave} = (A_{0°} + A_{90°})/2$, of the two orthogonal polarizations. **Figure 2A** shows that there is no significant difference between the results of the PEM and the average static polarization measurements with both showing absorption maxima near 1600 and 3000 cm^{-1}.

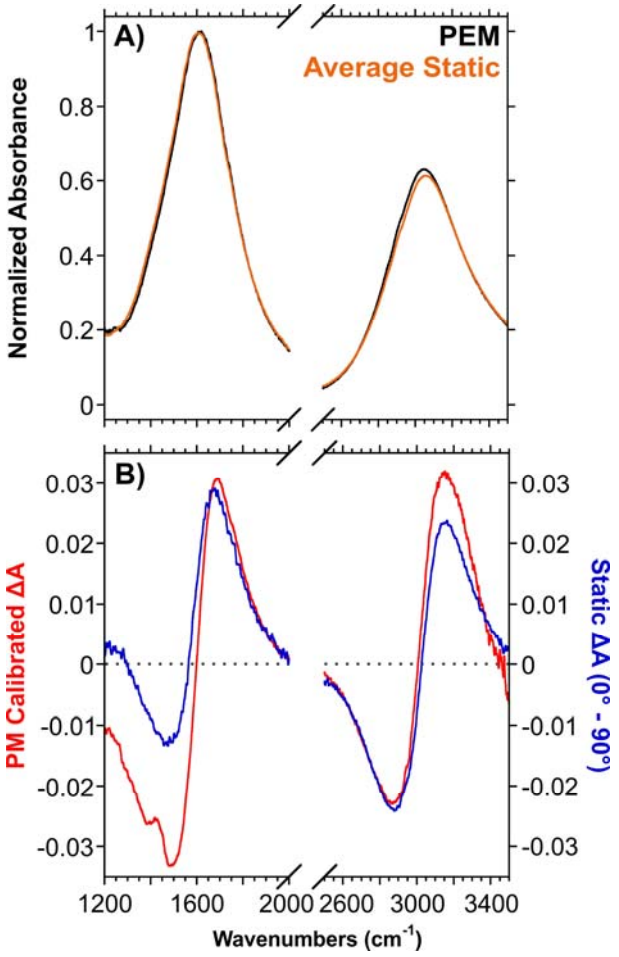

Figure 2. A) Comparison of the absorbance spectrum taken with the PEM (from the sum interferogram) and the average absorbance spectrum of the static polarization measurements (0 and 90°) from Figure 1. B) Comparison of the dichroic spectra obtained using the µPM-IRLD (with a modulation centered at λ = 1500 cm^{-1}) and the sequential measurement of $A_{0°}$ and $A_{90°}$. The µPM-IRLD spectrum is shown after calibration.

Quantitative ΔA spectra were obtained by calibrating the raw PM results and comparing it to the difference of the polarized absorbances. To calibrate the spectra, a linear polarizer was introduced with orientations that were parallel ($C_{\parallel}$) and perpendicular ($C_{\perp}$) to the polarizer positioned before the PEM. The spectra of I_{diff}/ I_{sum} for $C_{\parallel}$ and $C_{\perp}$ is shown in **Figure S1**. The calibrated difference spectrum can the obtained using equation (1):[53]

$$\Delta A = \log\left(\frac{C_{\perp}\left(\frac{G}{G'}C_{\parallel} - S\right)}{C_{\parallel}\left(\frac{G}{G'}C_{\perp} + S\right)}\right) \quad (1)$$

where G is the gain during the experimental measurements (10), and G' is the gain used during the calibration (2). **Figure 2B** shows the comparison between the calibrated spectrum and the result of $\Delta A = A_{0^\circ} - A_{90^\circ}$ obtained using the spectra of Figure 1B. Each resonance is split into two portions. The lower energy portion exhibits a negative ΔA value, and the higher energy a positive ΔA. Absolute values of ΔA are typically less than 4×10^{-2}. This response confirms that the three-branched second-order dendritic fractals exhibit an anisotropic character split into negative and positive contributions for both resonances. Although both spectra have similar intensities, the calibrated PM results have less noise than the spectrum obtained simply by subtracting the absorbances from the static polarization spectra. The response of going from negative to positive dichroism for $\Delta A = A_{0^\circ} - A_{90^\circ}$ was also established using finite-difference time domain (FDTD) calculations (**Figure S2**).

At the higher energy (HE) overlap, the enhancement of the EM field occurs only in the outermost structures (**Figure 3A, B**), whereas the lower energy (LE) overlap incorporated the structures from both the first and second-order generations (**Figure 3C, D**). This distribution has been previously related to the hybridization of the LSPRs associated with the incorporation of more structures with increasing generations.[41, 42]

Furthermore, the EM fields exhibit interesting anisotropy where different branches of the structure offer enhancement depending on the polarization direction. This is of importance once the surface is functionalized with an analyte as depending on the input polarization, the enhancement will occur in defined portions of the structure. Such localized effect can also be used for local photoinduced photoreactivity such as plasmon-mediated functionalization and polymerization of analytes. To date this has been demonstrated in the visible region,[35, 54]

however, such an approach could potentially be applied to mid-infrared resonances using highly tunable quantum cascade lasers.

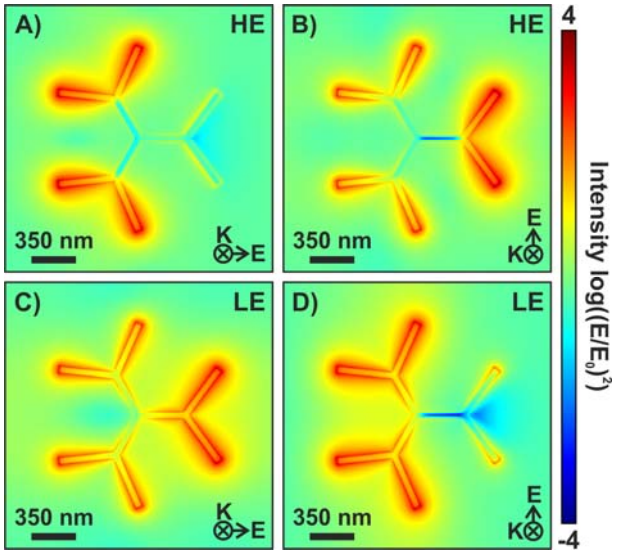

Figure 3. A-D) FDTD calculations of the electric field $(|E/E_0|)^2$: log scale representation at the high energy (HE) and low energy (LE) wavelengths where the absorbance spectra overlap at orthogonal polarizations for a second-order generation dendritic fractal composed of gold nanorods with side lengths of 350 nm.

2.3. Polarization-Modulation and Optical Tuning

As mentioned earlier, the optical properties of the dendritic fractals can be tuned by a variety of methods. The spectral positions of the resonances can be tuned by altering the size, and the number of inner branches. Coupling this tuning with expanding to higher-order generations allows for the incorporation of additional resonances. To explore how the PM measurements are influenced by each of these structural changes, additional dendritic fractals were studied.

2.3.1. Increasing the Side Lengths of the Nanorods in the Dendritic Fractals

Altering the dimensions of the fractal nanostructures is a practical way to tune the spectral position of their resonances, as was shown in previous studies where a 1 nm increase in the side length yields a red spectral shift of 6 to 7 nm.[41, 42] To demonstrate that this size

dependence continues with increasing side length, a narrow range of sizes (350-400 nm) were prepared such that the two LSPRs of the three-branched second-order generation were still located within the spectral range of interest. Additionally, structures with side lengths over 700 nm were also prepared with the aim of tuning the LSPR of the structures from the outermost branches within the lower energy region of interest.

The absorbance spectra of the structures with the smaller side lengths are shown in **Figure 4A**, and the longer side lengths are shown in **Figure S3A**. By increasing the side lengths, the dipolar mode attributed to the outermost branches appears in the fingerprint region of the mid-IR. Additionally, weaker absorptions were observed at higher energy, and are attributed to higher order modes (quadrupolar). The calibrated μPM-IRLD spectra (**Figure 4B**, **Figure S3B**) exhibit the characteristic modes associated with PM measurements of the three-branched second-order generation dendritic fractals. It is interesting to note that as the resonances shift to lower wavenumbers (lower energy), the relative ratio of the calibrated absorbance before and after $\Delta A = 0$ changes. This is attributed to the setting of the PEM controller to a fixed frequency of 1500 cm^{-1}. This frequency was selected as it lies at the center of the fingerprint region of the mid-IR. As expected, it was observed that both the resonances and the corresponding dichroic responses can be tuned based on the side length of the nanostructure. This is an important feature, particularly for SEIRA measurements, since it was demonstrated that maximum enhancement depends on the ratio of $\omega_{vib}/\omega_{res}$ where ω_{vib} is the frequency of the vibrational mode of the molecular species deposited onto the plasmonic surface and ω_{res} is the frequency of the LSPR. Specifically, it was shown that the ideal measurement is obtained when the ratio of $\omega_{vib}/\omega_{res} = 0.95$.[55]

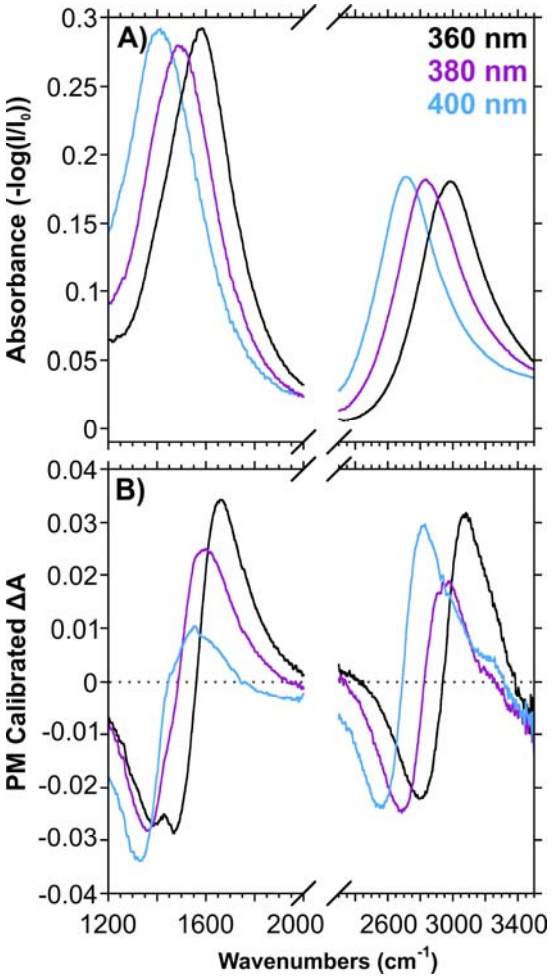

Figure 4. Effect of increasing the side length of the gold nanorods in the dendritic fractal on A) the absorbance, and B) the calibrated PM absorption spectra.

2.3.2. Increasing the Number of Inner Branches

A second means of tuning the LSPRs of the dendritic fractal is by increasing the number of inner branches (n), and in turn, the number of branches in higher-order generations (n – 1). Representative SEM images of the second-order dendritic fractals for varying the number of inner branches are shown as insets in **Figure 5A-C**. An advantage of increasing the number of branches is that it may allow for a greater density of hot-spots over the surface of the structure. For μPM-IRLD measurements, it is also likely that compared with the three-branched structures, increasing the number of branches is also likely to have varying effects on the polarization dependence.

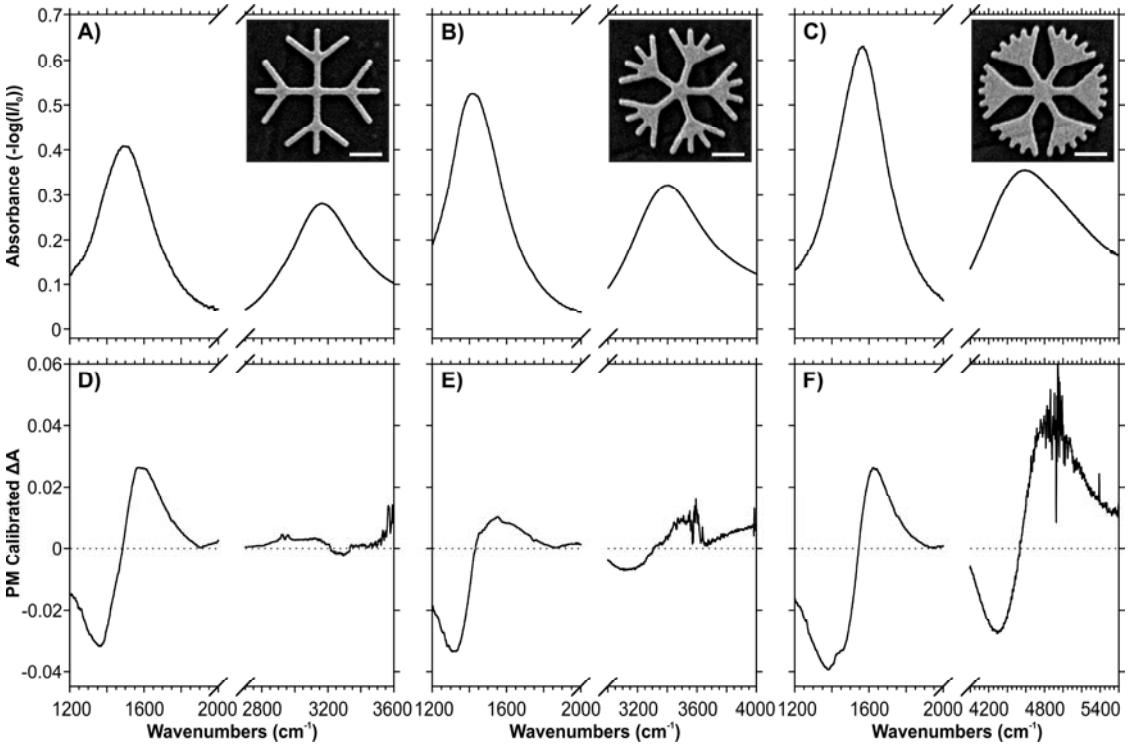

Figure 5. Influence of increasing the number of inner branches on the A-C) absorbance, and D-F) calibrated PM absorption spectra. Shown as insets in A-C) are SEM images corresponding to A) four-, B) five-, and C) six-branched second-order generation dendritic fractals. The scale bar of the inset images is 350 nm.

The absorbance spectra shown in Figure 5A-C all contain two LSPRs consistent with second-order generation dendritic fractals. As the number of inner branches increases, a noticeable blue-shift of the higher-energy resonance corresponding to the outermost structures is observed. Such observations have previously been reported for 3-dimensional multi-branched nanostructures.[56] As can be observed in the inset SEM images, increasing the number branches results in the branches becoming closer together. In the case of the six-branched structures, the branches are sufficiently close together that when prepared during the EBL process, a large portion of the branches are connected. This results in a small portion of the outerbranches being separated, resulting in a "duck foot"-like appearance. This decrease in exposed length may be the reason for the blue-shift of the higher-energy resonance, especially the larger shift going from five to six branches compared to going from four to five. Altering

the geometry of the nanorods, specifically the width, may help to minimize the duck foot structure.

The PM calibrated spectra also exhibit unique characteristics with increasing number of inner branches (**Figure 5D-F**). By definition, a structure that exhibits C4 symmetry (four-branched dendritic fractals), should not exhibit any anistropy. However, the μPM-IRLD measurements in Figure 5D shows a dichroic response for the LE resonance. The five- and six-branched structures (Figure 5E and F) exhibiting C5 and C6 symmetries exhibit a polarization dependence for both resonances, as shown by the dichroic responses. It is important to note that both spectra also exhibit spectral noise, that we believe is characteristic of modulating the PEM at 1500 cm^{-1}, as opposed to closer to the HE resonances at 3200 and 4600 cm^{-1}. This presence of spectral noise is evidenced by examining the calibrated μPM-IRLD spectrum obtained on CaF_2 (**Figure S4**).

To better understand the observed dichroism for the four-branched structures, FDTD calculations were performed to determine the spatial distribution of the enhancement (**Figure 6A, B**). Consistent with the calculations for the three-branched fractal (Figure 3), the HE resonance is localized to the outer branches (Figure 6A), while the LE resonance encorporates the inner and outer branches (Figure 6B), yielding the global response of the structure.

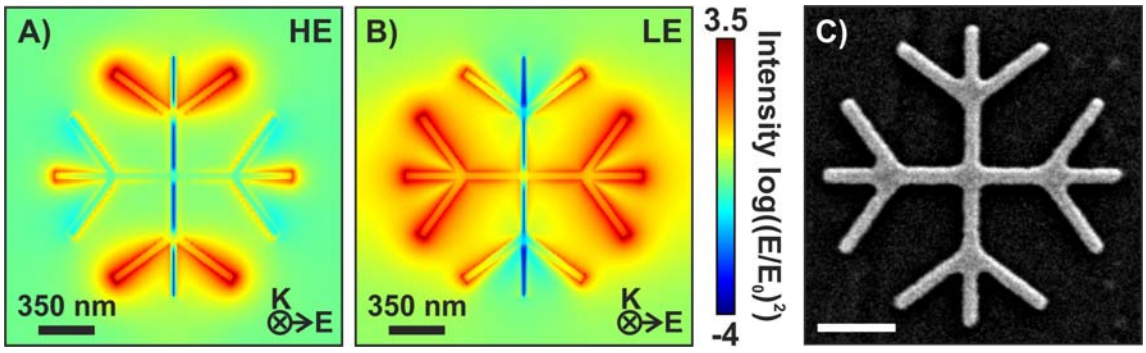

Figure 6. FDTD calculations of the electric field $(|E/E_0|)^2$: log scale representation at the A) high energy (HE) and B) low energy (LE) resonance wavelengths for a four-branched second-order generation dendritic fractal composed of gold nanorods with side lengths of 360 nm. C)

SEM image of the four-branched second-order dendritic fractal with side lengths of 360 nm. The scale bar in the SEM image is 350 nm.

There are two primary sources that can introduce nanoscale defects resulting in the introduction of a dichroic response. The first is the presence of polishing defects in the surface of the CaF_2 window (scratches), as best observed in Figure 1A. After fabrication, the fractals often overlap with the substrate defects, yielding nanoscale changes in the structure. The second, and more likely cause for a dichroic response is the presence of any differences in the dimensions of the nanorods along the *x* and *y*-axes. Based on the SEM image shown in **Figure 6C**, although written to be identical, the constituent nanorods do exhibit differences For example, the outermost structures, especially the angled branches, appear to have nanoscale differences in the lengths and widths. At the HE resonance, the dominant contribution is from the angled branches of the second-order generation. As the differences appear to exhibit some symmetry, it is likely that the dichroic response would be minimal. At the HE resonance, the inner branches play a role in the EM enhancement, along with a greater contribution from the central rods of the second-order generation. Since this resonance encorporates a greater portion of the structure, any anisotropy associated with the fabrication of the structure would result in a dichroic response of this resonance. In the case of the structure shown in Figure 6C, the total length along the y-axis (90° polarization) is approximately 7 nm longer than the total length along the x-axis (0° polarization). Although this difference may seem minimal, it is important to recognize that the μPM-IRLD measurements are performed on a 50 × 50 μm^2 array, containing 576 fractals in the case of this pattern. As such, a cumulative effect of the structural anisotropy will occur.

Overall, the results of the four-branched structure not only demonstrate the sensitivity of the μPM-IRLD measurements, but also the senstivity of the relationship between the interaction of light with plasmonic nanostructures.

2.3.3 Third-Order Generation Dendritic Fractals

As higher-order generations are fabricated, additional resonances are introduced. However, as the number of inner branches increases, it becomes more difficult to fabricate higher-order generations because the nanorods of the outermost generation overlap significantly. Once fabricated, a "duck foot"-like structure is observed. This effect can be minimized by truncating (removing branches) from the outer generation,[42] and/or altering the dimensions of the branches (i.e. increasing the length of the nanorods). With a particular interest in working with the intrinsic fractal, we have decided to not explore truncated fractals in this study. Furthermore, although increasing the length may work, the resulting red-shift of the resonances would likely lead to the loss structure's global LSPR due to substrate interfence above 1000 cm^{-1}. Therefore, we found that only structure that met our requirements was a three-branched, third-order generation dendritic fractal where the sidelengths were rather small (200 – 250 nm).

Included as an inset of **Figure 7A** is an SEM image of a three-branched third-order dendritic fractal with a side length 220 nm. As expected for this order-generation, three LSPRs were observed (Figure 6A), with two in the mid-IR (1600 and 2500 cm^{-1}) and one in the near-IR (5000 cm^{-1}). We focus here only on the anisotropy of the mid-IR resonances (**Figure 7B**). The anisotropy of the lower energy resonances is especially important as the electromagnetic field enhancement results from the whole or most of the structure as opposed to the highest energy resonance that is only derived from the outer-most branches. Specifically, the lowest energy resonance can be described as the global resonance of the structure, while the second lowest resonance incorporates the structures introduced in the second- and third-order generations. Once functionalized with an analyte, given equivalent enhancement, the greater the number of hot-spots present on the surface, the stronger the vibrational signal of the target molecule.

Consistent with the obtained results for the various three-branched second-order generation structures, the mid-infrared μPM-IRLD spectra indicate that the resonances are

anisotropic. As the structure maintains its C3 symmetry, this result can be explained due to the difference in total length of the structure along the 0 and 90 degree directions. Additionally, much like with what was observed in Figure 5, Figure 7B shows spectral noise introduced by modulating the PEM at 1500 cm^{-1}. However, as this noise lay outside of the spectral regions of interest, it was not necessary to choose a different modulation frequency.

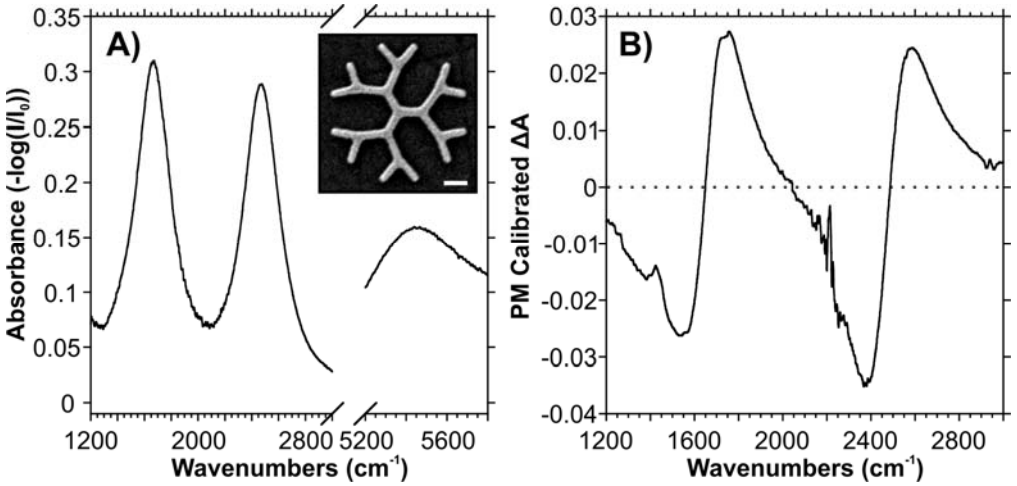

Figure 7. A) Absorbance and B) calibrated PM measurements for a three-branched third-order dendritic fractal. Included as an inset of A) in an SEM image of the structure with a scale bar of 200 nm.

2.4. Polarization-Modulated Surface-Enhanced Infrared Absorption

By tuning the position of the LSPRs of a structure(s), it is possible to enhance the vibrational fingerprint of a target located near the surface of the metal nanostructure. As previously mentioned, a ratio of 0.95 between the frequency of a vibrational mode and the resonance frequency maximizes the enhancement.[55] Owing to the incorporation of the PEM in these measurements, we will use the description of μPM-IRLD SEIRA for these results.

For the μPM-IRLD SEIRA measurements, the dendritic fractals were functionalized with a monolayer of 4-nitrothiophenol (4-NTP). 4-NTP is an ideal analyte for SEIRA measurements in the mid-IR as the vibrational fingerprint only contains a few peaks in the fingerprint region that can be readily assigned. In both the absorbance and PM calibrated

spectra (**Figure 8A, B**), dips are observed for the vibrational modes of 4-NTP. By subtracting the baseline from the spectra, the vibrational intensities associated with 4-NTP can be obtained (**Figure 8C, D**). The peaks near 1340 and 1515 cm^{-1} can be assigned to the symmetric and asymmetric NO_2 modes, and those near 1570 and 1590 cm^{-1} correspond to the ring modes.[57, 58] Furthermore, the mode at 1340 cm^{-1} has an asymmetric shape, characteristic of a Fano resonance. This type of resonance occurs when the frequency of the plasmon resonance associated with the structure matches the vibrational frequency of the analyte. As the sizes of the structures were specifically tuned to be near 1340 cm^{-1}, this is the vibrational mode that would experience the greatest enhancement, and therefore exhibit the greatest Fano line shape. Importantly, the μPM-IRLD SEIRA spectrum (Figure 8D) exhibits a similar spectrum to that of the traditional SEIRA spectrum (Figure 8C), with the 4-NTP peaks appearing in similar positions. Although the intensity of the peaks is quite weak, it is important to recognize that these measurements were performed with only a monolayer (or less) of the 4-NTP present on the gold surface.

As was previously demonstrated, it is possible to tune the position of the dip in the μPM-IRLD spectra by varying the size. To explore how the position of the change in dichroism influences this μPM-IRLD SEIRA measurements, a series of second-order generation three-branched dendritic fractals were prepared, with side lengths varying from 360 to 460 nm (**Figure 8E**). Although a value of 0.95 for the ratio of $\omega_{vib}/\omega_{dip}$ (equivalent to $\omega_{vib}/\omega_{res}$) was obtained for 380 nm, and did yield the strongest response (**Figure 8F**), a new distribution for intensity was observed. As the frequency of $\Delta A = 0$ approached the vibrational frequency position of the symmetric NO_2 mode, the integrated peak area decreased (Figure 8E), and then proceeded to increase once past the vibrational mode. This observation is unique compared to the previously mentioned study where the enhancement with respect to $\omega_{vib}/\omega_{res}$ was observed to follow a Lorentzian fit.[55] Here, we attribute this difference to the fundamental differences between SEIRA and μPM-IRLD SEIRA measurements. In μPM-

IRLD measurements, a ΔA between two orthogonal polarizations is reported, and has been mentioned, ΔA = 0 occurs at the average absorbance of both polarizations, whereas only a single polarization is typically used in SEIRA experiments. The FDTD calculations of Figure 3 showed that no one polarization offered significantly greater electromagnetic enhancement or spatial distribution at the frequency of overlap. Therefore, once functionalized with an analyte, we would expect that both polarizations would exhibit similar Fano resonances, thus when the difference is taken, little to no signal would be observed. Additionally, unlike the SEIRA results where a single maxima is observed, the μPM-IRLD SEIRA measurements show two local maxima. One of the maxima is observed as a negative dichroism ($A_{0°} < A_{90°}$) and the other as positive dichroism ($A_{0°} > A_{90°}$). Both of these maxima can be used to strongly enhance the vibrational signal (Figure 8E and F), thus leading to measurements that offer enhanced sensitivity. These maxima occur at the positions where the two absorbance spectra exhibit the greatest differences. It is important to note that these do not correspond to the individual absorbance maxima for each polarization. Therefore, when performing μPM-IRLD SEIRA measurements it is important to tune the positions of these maxima so that they are in relevant positions, while also positioning $\Delta A = 0$ in a spectral domain void of vibrational modes of interest. As this is difficult to achieve in the fingerprint region, we propose that the fabrication of a series of structures (as was performed in this study) is ideal.

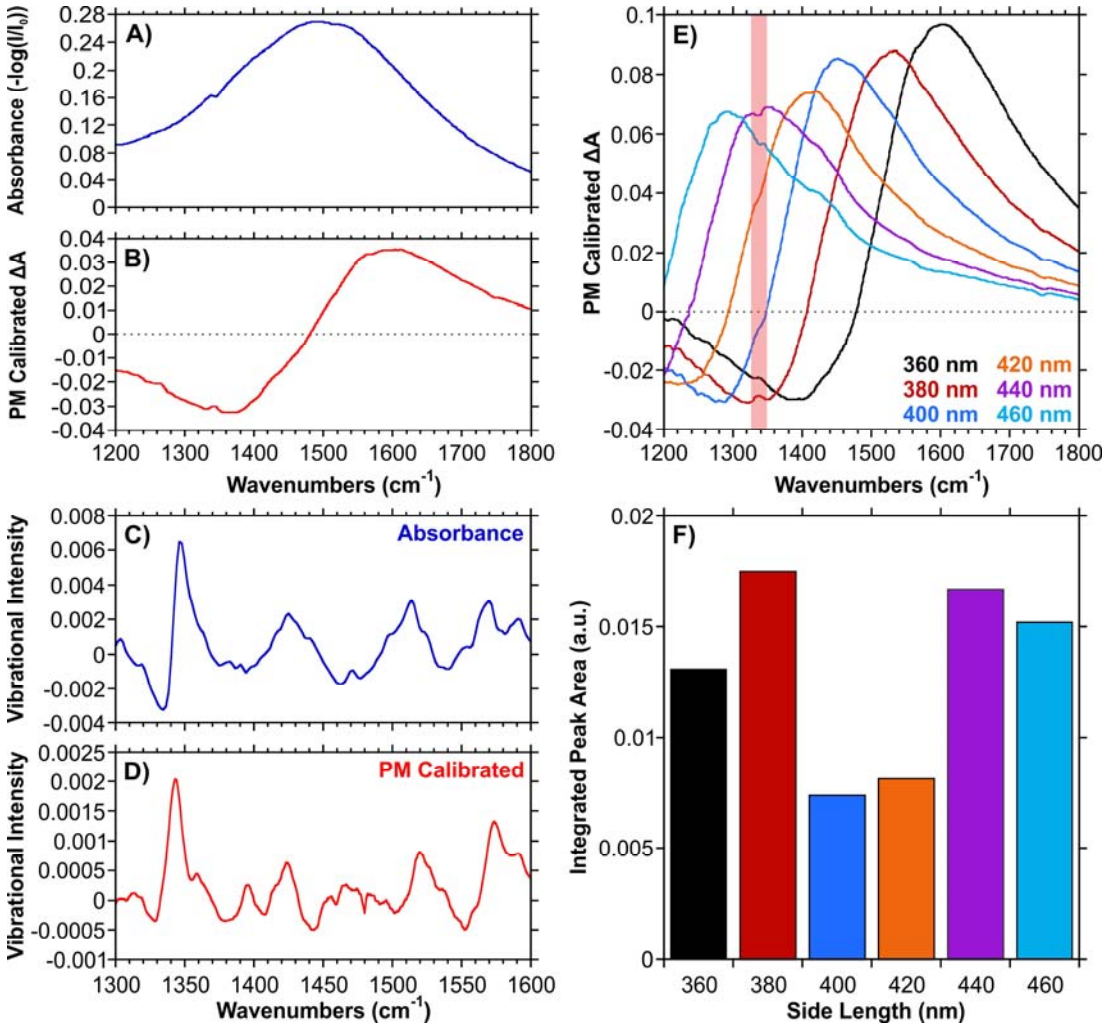

Figure 8. A) Absorbance and B) PM calibrated measurements of a 4-NTP functionalized sample (three-branched second-order generation). Vibrational intensity spectra obtained from C) the absorbance spectrum, and D) the PM calibrated spectrum. E) PM calibrated spectra for a series of three-branched second-order dendritic fractals functionalized with 4-NTP, and F) the corresponding integrated peak area from 1328 – 1346 cm^{-1}, corresponding to the symmetric NO_2 stretch as indicated by the shaded region of E).

3. Conclusion

We have demonstrated that polarization-modulated measurements can be readily coupled with plasmonic nanostructures for probing the optical properties of the structure in the mid-IR. The LSPRs of dendritic fractals do exhibit orthogonal polarization dependence in

the mid-IR, and are therefore an ideal set of structures for PM measurements. Since the difference between the orthogonally polarized absorbances is small, calibrated PM-IRLD measurements yielded the absolute dichroic response over a large spectral range showing negative and positive dichroic responses centered around the maximum resonance. By increasing the side lengths of the constituent nanorods or their symmetrical arrangement, it is possible to accurately tune the spectral position of the resonances and respective linear dichroism to spectroscopically relevant regions in the mid-IR. With sufficient tuning of the structure, such that the LSPR spectral position is near the vibrational frequency of an analyte, and that the maximum dichroism occurs in a spectral region void of vibrational modes, it is possible to detect an analyte of interest by SEIRA.

Furthermore, the incorporation of analytes that exhibit linear dichroism to the measurements could potentially enable surface-enhanced vibrational linear dichroism studies in the mid-IR. Such studies could then be used to probe surface-sensitive reactions at low concentrations. Lastly, due to the radial nature of the dendritic fractals, surface-enhanced vibrational circular dichroism may also be possible by tailoring the chiroptical properties of the fractal structures.[22]

4. Experimental Section

Electron-Beam Lithography: The procedure for the fabrication of the nanostructures by EBL was performed using similar methodologies to our previous work involving SEIRA and the mid-infrared beamline at the CLS.[26, 42] CaF_2 windows (12 mm diameter × 2 mm, Spectral Systems LLC, Hopewell Junction, NY) were first cleaned by UV-Ozone for 30 min to ensure adhesion of the thin film of resist. The cleaned substrates were then coated with a 100 nm thick layer of poly(methyl methacrylate) (PMMA, A2 950 resist (MicroChem Corp., Westborough, MA)). Subsequently, a thin layer of AquaSave (10s of nm) (Mitsubishi Rayon America Inc., New York, NY) was subsequently applied to the PMMA coated substrate. A Leo Zeiss 1530 SEM was used to perform all EBL using a 30 kV EHT acceleration voltage

and a 10 μm aperture. An area exposure dose of 260 μC cm^{-2} was used for the writing of each structure. Each pattern was written as a patch of structures covering an area of 50 × 50 $μm^2$. Following exposure, the exposed substrates were placed into developing solutions (water to remove AquaSave, and 1:3 methyl isobutyl ketone:isopropanol (Microchem Corp., Westborough, MA)) to remove the exposed resist, and dried under air. Electron-beam evaporation was then used to deposit a 3 nm adhesion layer of titanium followed by a 20 nm layer of gold. Both metals were deposited at a rate no greater than 0.5 Å s^{-1}. The remaining PMMA was removed by placing the samples into acetone (CHROMASOLV, Sigma-Aldrich, St. Louis, MO). Scanning electron micrographs of the fabricated platforms were collected with the 1530 SEM. Prior to imaging the structures, the sample was coated with 5 nm of osmium. The sample used for imaging was one of the samples used to acquire the μPM-IRLD spectra.

Static Polarization Infrared Measurements: Fourier transform infrared (FT-IR) microspectroscopy measurements were performed at the Mid-IR beamline synchrotron facility located at the Canadian Light Source (Beamline 01B-01). The beamline end station consists of a Bruker Optics Vertex 70v FT-IR spectrometer coupled to a Hyperion 3000 IR Microscope (Bruker Optics, Billerica, MA, USA). Light was focused and collected in absorbance mode using a 36× objective (NA 0.65). The input source coming from the synchrotron was linearly polarized. The collected light was measured using a narrowband fast DC coupled mercury cadmium telluride (MCT) (liquid nitrogen cooled) Kolmar (Kolmar Technologies, Inc., Newburyport, MA, USA) detector. Measurements were collected from 8000 to 800 cm^{-1} with a spectral resolution of 4 cm^{-1}. Each spectrum is the average of 512 spectra.

Polarization-Modulated Infrared Linear Dichroism Microscopy Measurements: The same beamline, spectrometer, and microscope were used for the polarization-modulation (PM) measurements, with the following alterations. The general configuration of the PM set-up is

similar to the one described by Schmidt *et al*,[49] and is shown in **Figure S5**. In the new set-up, a photoelastic modulator (PEM, Hinds Instruments Inc., Hillsboro, OR, USA) was placed after the polarizer, and was positioned at a 45° angle relative to the polarizer. This portion of the set-up is contained within a purged polycarbonate box to minimize the presence of atmospheric water vapor. The PEM optical head is linked to the controller (Hinds Instruments PEM-100 Controller). The signal obtained from the MCT is then sent to a synchronous sampling demodulator (SSD 100, GWC Technologies, Madison, WI, USA). The difference and sum interferograms are obtained from this demodulator through two separate channels and undergo Fourier transformation. The ratio of the difference and sum is then calculated prior to calibration. To perform the calibration measurements, a polarizer is placed after the sample and oriented along the parallel ($C\parallel$) and perpendicular ($C\perp$) with respect to the first polarizer placed before the PEM. The two acquired polarized calibration files are then used in equation 1 to provide a quantitative ΔA value.

Surface-Enhanced Infrared Absorption: For the μPM-IRLD SEIRA measurements, the samples were functionalized for 6 h in a freshly prepared 10^{-3} M solution of 4-nitrothiophenol (4-NTP) (Sigma-Aldrich, St. Louis, MO) prepared in ethanol. After 6 h, the functionalized sample was dipped in ethanol to remove any unbound 4-NTP and was dried under air. PM-SEIRA spectra were then collected using the parameters previously mentioned.

Electromagnetic Field Modelling: Finite difference time domain (FDTD) modelling (Lumerical) was used to simulate the absorption and electromagnetic fields of the dendritic fractals. The lengths of the individual nanorods are those described in the text, with widths of 50 nm, heights of 20 nm for gold, and 3 nm of titanium placed beneath the gold. Palik dielectric values for gold and titanium were used for the FDTD calculations.[59] The structures were placed on a substrate with a constant refractive index of 1.42 representing the CaF_2 window. Periodic boundary conditions on the *x*- and *y*-axes conditions were no smaller than 700 nm and were representative of the periodicity of the fabricated structures. Last, a

perfectly matched layer (PML) was used in the *z*-axis. Mesh sizes of 7.5 nm were used in the *x*- and *y*-axes and 3 nm in the z-axis.

Supporting Information
Supporting Information is available from the Wiley Online Library or from the author.

Acknowledgements

The authors gratefully acknowledge the Nanofabrication Facility at Western University. This research was supported by the Natural Sciences and Engineering Council (NSERC) of Canada. This research was further funded by the Canada Research Chairs program in "Photonics and Nanosciences (F.L-L.). G.Q.W. thanks NSERC for the post-graduate scholarship doctoral (PGS-D) and acknowledges the receipt of support from the CLS Graduate and Post-Doctoral Student Travel Support Program. D.M.M. thanks the Ontario government for a Queen Elizabeth II Graduate Scholarship in Science and Technology. Research described in this work was performed at the Mid-Infrared Spectromicroscopy (01B1-1) Beamline at the Canadian Light Source, which is supported by the Canada Foundation for Innovation, NSERC, the University of Saskatchewan, the Government of Saskatchewan, Western Economic Diversification, the National Research Council Canada, and the Canadian Institutes of Health Research.

Conflict of Interest
The authors declare no conflict of interest.

Received: ((will be filled in by the editorial staff))
Revised: ((will be filled in by the editorial staff))
Published online: ((will be filled in by the editorial staff))

References

1. Snell, K. E.; Hou, R.; Ishow, E.; Lagugné-Labarthet, F., *Langmuir* **2015,** *31*, 7296.
2. Laventure, A.; Bourotte, J.; Vapaavuori, J.; Karperien, L.; Sabat, R. G.; Lebel, O.; Pellerin, C., *ACS Appl. Mater. Interfaces* **2017,** *9*, 798.
3. Zhang, G.; Li, J.; Cui, P.; Wang, T.; Jiang, J.; Prezhdo, O. V., *J. Phys. Chem. Lett.* **2017,** *8*, 1031.
4. Bulheller, B. M.; Rodger, A.; Hicks, M. R.; Dafforn, T. R.; Serpell, L. C.; Marshall, K. E.; Bromley, E. H. C.; King, P. J. S.; Channon, K. J.; Woolfson, D. N.; Hirst, J. D., *J. Am. Chem. Soc.* **2009,** *131*, 13305.
5. Guardingo, M.; Bellido, E.; Miralles-Llumà, R.; Faraudo, J.; Sedó, J.; Tatay, S.; Verdaguer, A.; Busqué, F.; Ruiz-Molina, D., *Small* **2014,** *10*, 1594.
6. Sang, L.; Mudalige, A.; Sigdel, A. K.; Giordano, A. J.; Marder, S. R.; Berry, J. J.; Pemberton, J. E., *Langmuir* **2015,** *31*, 5603.
7. Lobo Maza, F.; Méndez De Leo, L.; Rubert, A. A.; Carro, P.; Salvarezza, R. C.; Vericat, C., *J. Phys. Chem. C* **2016,** *120*, 14597.
8. Lee, H.; Kim, J. H.; Dhakal, K. P.; Lee, J. W.; Jung, J. S.; Joo, J.; Kim, J., *Appl. Phys. Lett.* **2012,** *101*, 113103.

9. Al-Atar, U.; Bokov, A. A.; Marshall, D.; Teichman, J. M. H.; Gates, B. D.; Ye, Z.-G.; Branda, N. R., *Chem . Mater.* **2010,** *22*, 1318.
10. Wen, W.; Zhu, Y.; Liu, X.; Hsu, H.-P.; Fei, Z.; Chen, Y.; Wang, X.; Zhang, M.; Lin, K.-H.; Huang, F.-S.; Wang, Y.-P.; Huang, Y.-S.; Ho, C.-H.; Tan, P.-H.; Jin, C.; Xie, L., *Small* **2017,** *13*, 1603788.
11. Zhang, S.; Mao, N.; Zhang, N.; Wu, J.; Tong, L.; Zhang, J., *ACS Nano* **2017,** *11*, 10366.
12. Lin, J.; Liang, L.; Ling, X.; Zhang, S.; Mao, N.; Zhang, N.; Sumpter, B. G.; Meunier, V.; Tong, L.; Zhang, J., *J. Am. Chem. Soc.* **2015,** *137*, 15511.
13. Ivanovski, V.; Mayerhöfer, T. G.; Kriltz, A.; Popp, J., *Spectrochim. Acta Mol. Biomol. Spectrosc.* **2017,** *173*, 608.
14. Kharintsev, S. S.; Shukhina, K. L.; Fishman, A. I.; Saikin, S. K., *J. Mater. Chem. C* **2017,** *5*, 6828.
15. Hong, Y.; Zhou, H.; Qian, W.; Zuo, B.; Wang, X., *J. Phys. Chem. C* **2017,** *121*, 19816.
16. Nihonyanagi, S.; Yamaguchi, S.; Tahara, T., *Chem. Rev.* **2017,** *117*, 10665.
17. Schaefer, J.; Gonella, G.; Bonn, M.; Backus, E. H. G., *Phys. Chem. Chem. Phys.* **2017,** *19*, 16875.
18. Gansel, J. K.; Thiel, M.; Rill, M. S.; Decker, M.; Bade, K.; Saile, V.; von Freymann, G.; Linden, S.; Wegener, M., *Science* **2009,** *325*, 1513.
19. Hu, J.; Zhao, X.; Li, R.; Zhu, A.; Chen, L.; Lin, Y.; Cao, B.; Zhu, X.; Wang, C., *Opt. Express* **2016,** *24*, 11023.
20. Kong, X.-T.; Zhao, R.; Wang, Z.; Govorov, A. O., *Nano Lett.* **2017,** *17*, 5099.
21. Hentschel, M.; Schäferling, M.; Duan, X.; Giessen, H.; Liu, N., *Sci. Adv.* **2017,** *3*.
22. Luo, Y.; Chi, C.; Jiang, M.; Li, R.; Zu, S.; Li, Y.; Fang, Z., *Adv. Opt. Mater.* **2017,** *5*, 1700040.
23. Wang, X.; Tang, Z., *Small* **2017,** *13*, 1601115.
24. D'Andrea, C.; Bochterle, J.; Toma, A.; Huck, C.; Neubrech, F.; Messina, E.; Fazio, B.; Maragò, O. M.; Di Fabrizio, E.; Lamy de La Chapelle, M.; Gucciardi, P. G.; Pucci, A., *ACS Nano* **2013,** *7*, 3522.
25. Thomas, R.; Swathi, R. S., *J. Phys. Chem. C* **2016,** *120*, 18733.
26. Wallace, G. Q.; Tabatabaei, M.; Hou, R.; Coady, M. J.; Norton, P. R.; Simpson, T. S.; Rosendahl, S. M.; Merlen, A.; Lagugné-Labarthet, F., *ACS Photonics* **2016,** *3*, 1723.
27. Chen, X.; Wang, C.; Yao, Y.; Wang, C., *ACS Nano* **2017,** *11*, 8034.
28. Aouani, H.; Šípová, H.; Rahmani, M.; Navarro-Cia, M.; Hegnerová, K.; Homola, J.; Hong, M.; Maier, S. A., *ACS Nano* **2013,** *7*, 669.
29. Cerjan, B.; Yang, X.; Nordlander, P.; Halas, N. J., *ACS Photonics* **2016,** *3*, 354.
30. Cetin, A. E.; Turkmen, M.; Aksu, S.; Etezadi, D.; Altug, H., *Appl. Phys. B* **2015,** *118*, 29.
31. Aslan, E.; Aslan, E.; Turkmen, M.; Saracoglu, O. G., *Sens. Actuator A Phys.* **2017,** *267*, 60.
32. Limaj, O.; Etezadi, D.; Wittenberg, N. J.; Rodrigo, D.; Yoo, D.; Oh, S.-H.; Altug, H., *Nano Lett.* **2016,** *16*, 1502.
33. Etezadi, D.; Warner Iv, J. B.; Ruggeri, F. S.; Dietler, G.; Lashuel, H. A.; Altug, H., *Light Sci. Appl.* **2017,** *6*, e17029.
34. Chen, K.; Adato, R.; Altug, H., *ACS Nano* **2012,** *6*, 7998.
35. Tijunelyte, I.; Kherbouche, I.; Gam-Derouich, S.; Nguyen, M.; Lidgi-Guigui, N.; de la Chapelle, M. L.; Lamouri, A.; Levi, G.; Aubard, J.; Chevillot-Biraud, A.; Mangeney, C.; Felidj, N., *Nanoscale Horiz.* **2017,** 10.1039/C7NH00113D.
36. Song, Y.; Tran, V. T.; Lee, J., *ACS Appl. Mater. Interfaces* **2017,** *9*, 24433.
37. Grant, J.; McCrindle, I. J. H.; Cumming, D. R. S., *Opt. Express* **2016,** *24*, 3451.

38. Nesterov, M. L.; Yin, X.; Schäferling, M.; Giessen, H.; Weiss, T., *ACS Photonics* **2016,** *3*, 578.
39. Besteiro, L. V.; Zhang, H.; Plain, J.; Markovich, G.; Wang, Z.; Govorov, A. O., *Adv. Opt. Mater.* **2017,** *5*, 1700069.
40. Zhang, W.; Wu, T.; Wang, R.; Zhang, X., *J. Phys. Chem. C* **2017,** *121*, 666.
41. Gottheim, S.; Zhang, H.; Govorov, A. O.; Halas, N. J., *ACS Nano* **2015,** *9*, 3284.
42. Wallace, G. Q.; Foy, H. C.; Rosendahl, S. M.; Lagugné-Labarthet, F., *J. Phys. Chem. C* **2017,** *121*, 9497.
43. Green, M. J.; Barner, B. J.; Corn, R. M., *Rev. Sci. Instrum.* **1991,** *62*, 1426.
44. Barner, B. J.; Green, M. J.; Saez, E. I.; Corn, R. M., *Anal. Chem.* **1991,** *63*, 55.
45. Buffeteau, T.; Desbat, B.; Turlet, J. M., *Appl. Spectrosc.* **1991,** *45*, 380.
46. Blaudez, D.; Turlet, J.-M.; Dufourcq, J.; Bard, D.; Buffeteau, T.; Desbat, B., *J. Chem. Soc., Faraday Trans.* **1996,** *92*, 525.
47. Buffeteau, T.; Pézolet, M., *Appl. Spectrosc.* **1996,** *50*, 948.
48. Cornut, I.; Desbat, B.; Turlet, J. M.; Dufourcq, J., *Biophys. J.* **1996,** *70*, 305.
49. Schmidt, M.; Schade, U.; Grunze, M., *Infrared Phys. Technol.* **2006,** *49*, 69.
50. Schmidt, M.; Gierlinger, N.; Schade, U.; Rogge, T.; Grunze, M., *Biopolym.* **2006,** *83*, 546.
51. Schmidt, M.; Lee, J. S.; Schade, U., *Infrared Phys. Technol.* **2010,** *53*, 157.
52. Santoro, G.; Schmidt, M.; Schade, U.; Marco, C.; Ellis, G., *J. Phys. Conf. Ser.* **2012,** *359*, 012005.
53. Pézolet, M.; Pellerin, C.; Prud'homme, R. E.; Buffeteau, T., *Vib. Spectrosc.* **1998,** *18*, 103.
54. Nguyen, M.; Kherbouche, I.; Gam-Derouich, S.; Ragheb, I.; Lau-Truong, S.; Lamouri, A.; Levi, G.; Aubard, J.; Decorse, P.; Felidj, N.; Mangeney, C., *Chem. Commun.* **2017,** *53*, 11364.
55. Vogt, J.; Huck, C.; Neubrech, F.; Toma, A.; Gerbert, D.; Pucci, A., *Phys. Chem. Chem. Phys.* **2015,** *17*, 21169.
56. Chirumamilla, M.; Chirumamilla, A.; Roberts, A. S.; Zaccaria, R. P.; De Angelis, F.; Kjær Kristensen, P.; Krahne, R.; Bozhevolnyi, S. I.; Pedersen, K.; Toma, A., *Adv. Opt. Mater.* **2017,** *5*, 1600836.
57. Zhang, Z.; Imae, T., *J. Colloid Interface Sci.* **2001,** *233*, 99.
58. Merklin, G. T.; He, L.-T.; Griffiths, P. R., *Appl. Spectrosc.* **1999,** *53*, 1448.
59. Palik, E. D., In *Handbook of Optical Constants of Solids*, Academic Press: Burlington, 1997.

Short summary and table of content graphic.

Exploiting Anisotropy of Plasmonic Nanostructures with Polarization-Modulation Infrared Linear Dichroism Microscopy (μPM-IRLD).

Gregory Q. Wallace, Stuart T. Read, Danielle M. McRae, Scott M. Rosendahl, and François Lagugné-Labarthet*

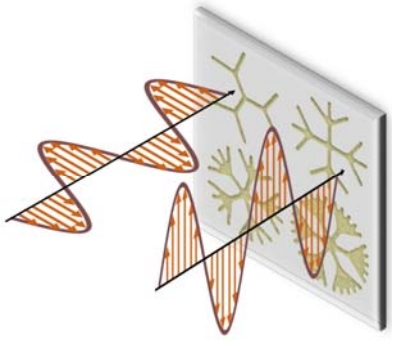

Polarization-modulated infrared linear dichroism microscopy uses mid-infrared light with orthogonal polarizations to excite the localized surface plasmon resonances of metallic nanostructures. Doing so allows for detecting the anisotropy of the plasmon resonances that are later applied to enhancing the infrared vibrational fingerprint of an adsorbed analyte.

Supporting Information

Exploiting Anisotropy of Plasmonic Nanostructures with Polarization-Modulation Infrared Linear Dichroism Microscopy (μPM-IRLD).

*Gregory Q. Wallace, Stuart T. Read, Danielle M. McRae, Scott M. Rosendahl, and François Lagugné-Labarthet**

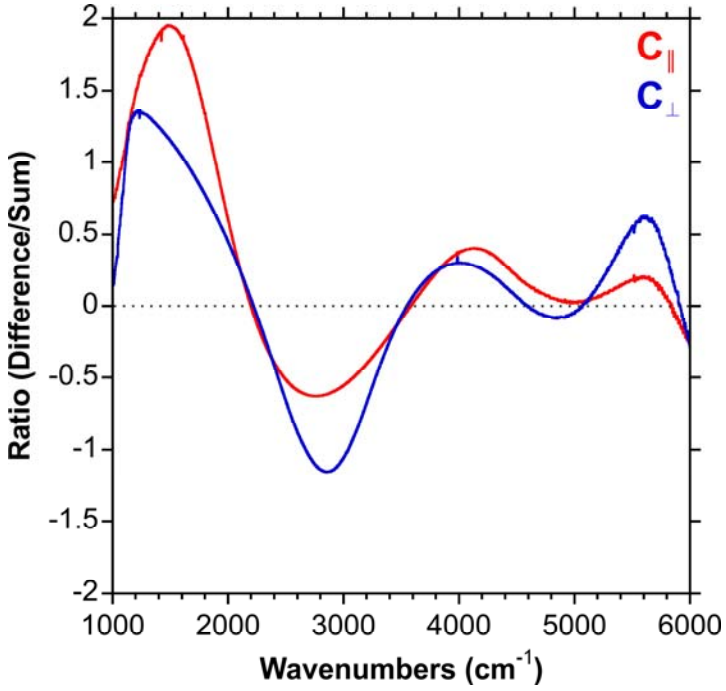

Figure S1. Raw PM absorption ratio spectra needed to perform the calibration. These were obtained by introducing a polarizer that was positioned parallel (Cpp) or perpendicular (Cps) with respect to the polarizer direction positioned in front of the PEM.

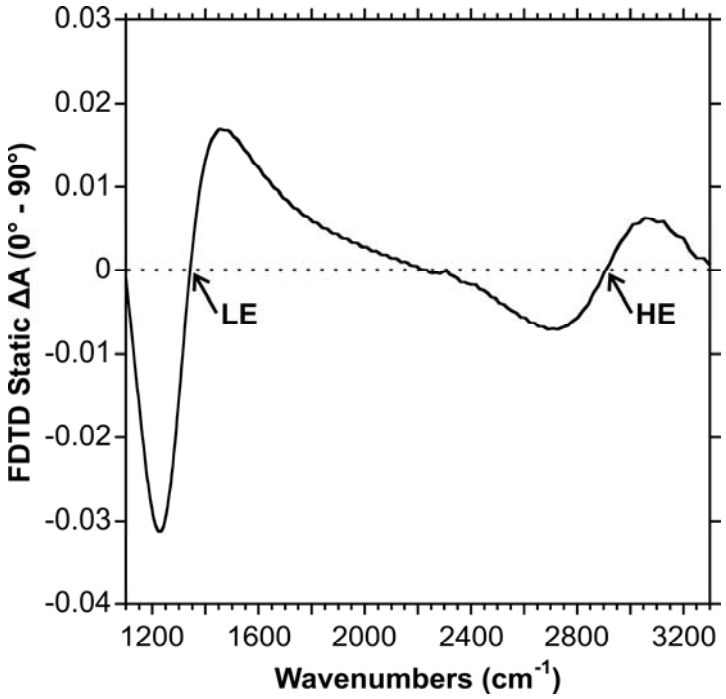

Figure S2. Calculated dichroic spectrum from FDTD calculations. The points indicated by LE and HE correspond to the low energy and high energy positions used to generate the EM field maps in Figure 3.

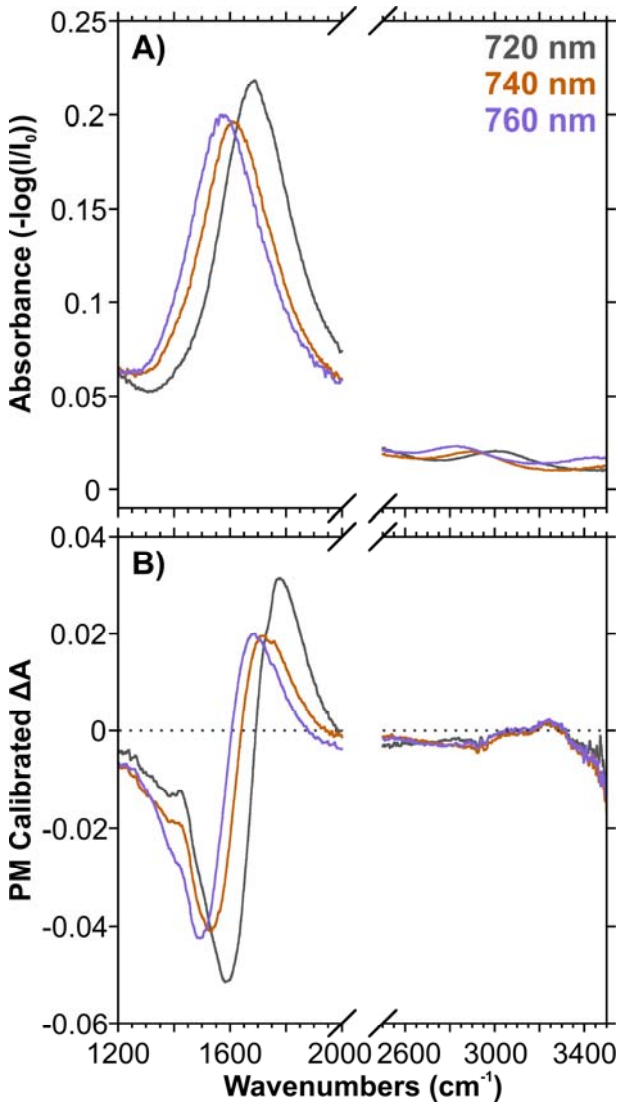

Figure S3. Effect of significantly increasing the side length of the gold nanorods in the three-branched second-order generation dendritic fractal on A) the absorbance, and B) the calibrated PM absorption spectra.

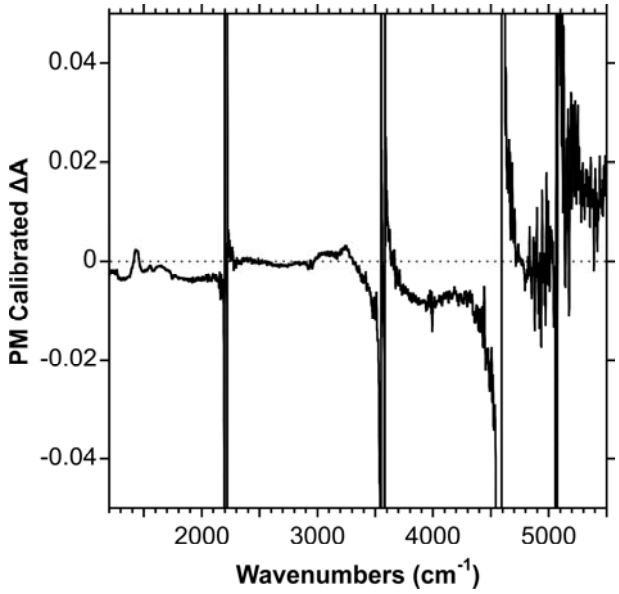

Figure S4. Calibrated PM spectrum obtained on CaF_2.

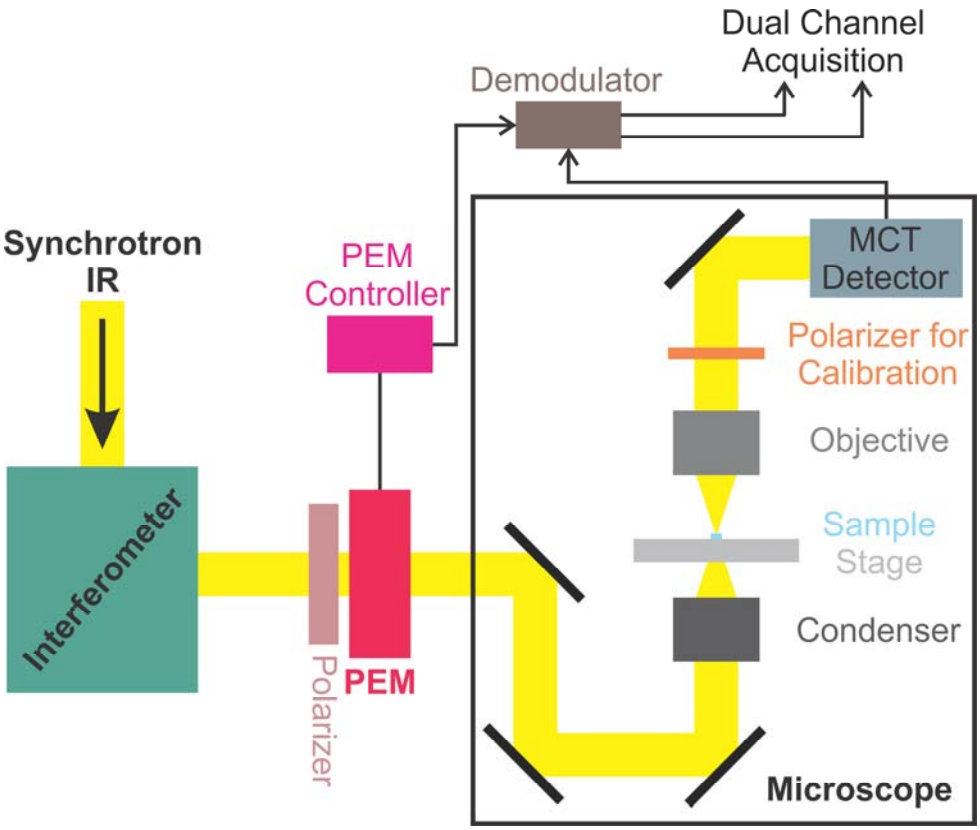

Figure S5. General schematic of the set-up used to perform the PM measurements.